Proceedings of ETCE/OMAE2000 Joint Conference
Energy for the New Millenium
February 14-17, 2000, New Orleans, LA, USA

ETCE/OMAE2000-6144

NON-GAUSSIAN AIRGAP RESPONSE MODELS FOR FLOATING STRUCTURES

Bert Sweetman
Department of Civil & Env. Engr.
Stanford University
Stanford, California 94305-4020
Email: sweetman@leland.stanford.edu

Steven R. Winterstein
Department of Civil & Env. Engr.
Stanford University
Stanford, California 94305-4020
Email: Steven.Winterstein@stanford.edu

Abstract

The air gap response of a specific semi-submersible platform subjected to irregular waves is considered. Detailed model tests for this structure are studied. Both motions and air gap time-histories are available: statistical analyses are performed both for the absolute near-structure wave elevation (with respect to a fixed observer), and the relative wave elevation (with respect to the moving structure). Several probabilistic models are studied to predict these near-structure wave elevations: a linear diffraction model typical of standard practice, and several new hybrid model that include second-order effects in the incident wave, but not in the diffracted wave. The first of these hybrid models is moment-based, while the second relies on narrow-band theory. Either model can be implemented in place of the standard linear-only model with little additional computational effort, as only linear diffraction analysis is required. Both models are found to better predict the airgap demand than standard linear diffraction analysis.

Introduction and Background

While air gap modeling is of concern for both fixed and floating structures, it is particularly challenging in the case of floating structures because of their large volumes and the resulting effects of wave diffraction and radiation. Both effects are considered here, but the primary focus is on the local wave elevation, which is believed to be the most challenging step to predict the air gap response.

Existing practice for calculating design air gap levels for fixed platforms employ a design wave approach based on the 100-year extreme wave crest level. Jacket structures, which predominate in many geographical areas, are slender relative to the length of the incident waves and so experience only small diffraction effects. Thus, application of the design wave approach is reasonable to the extent that the global structural behavior is quasi-static.

Higher volume, fixed, gravity base structures further complicate the air gap calculation by significantly diffracting the incident waves. For these structures ignoring diffraction effects is non-conservative in that diffraction effects generally worsen the air gap demand.

Large-volume floating structures including semi-submersibles and floating production, storage and offloading vessels (FPSO's) offer the most significant challenge. Large-volume submerged bodies give rise to two distinct effects: (1) global forces and resulting motions are significantly affected by diffraction; and (2) the local wave elevation, $\eta(t)$, is also significantly influenced by diffraction and refraction. These wave amplification effects are most extreme at locations above a pontoon and/or near a major column.

Increased global motions tend to reduce air gap demand in that the vessel is able to comply with the changing water free-surface level, i.e. to float over large waves. Diffraction and refraction effects, however, tend to increase the air-gap demand. Both effects are important in air gap prediction: how high the waves rise, and how much the deck translates vertically (due to heave, pitch and roll) both need to be known as functions of time at a given point to predict possible wave impact with the deck.

Present air gap design methodologies for floating structures are not standard and rely heavily on empirical knowledge and

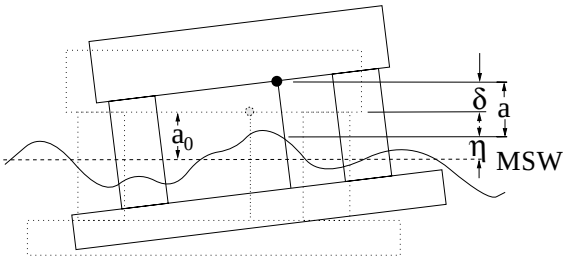

Figure 1. Airgap Variable Definitions

model tests. Most of the experience with semi-submersibles has been in support of the drilling industry. Drilling operations are extremely sensitive to vertical vessel motions, and drilling semi-submersibles are designed to accommodate that sensitivity during normal operating conditions. During extreme storms, however, drilling vessels generally suspend drilling and ballast up to a (shallower) survival draft. In extreme cases, these vessels may leave location until the weather becomes more benign.

Large production semi-submersibles and the Mobile Offshore Base (MOB) provide design challenges that are well outside the present design experience base. These vessels are significantly larger than drilling semisubmersible platforms and are generally required to remain on station throughout the most severe weather. The absence of significant empirical knowledge relevant to these new vessels further heightens the need for a firm theoretical understanding of the air gap phenomenon. Urgency is added by the fact that air gap design problems (wave impacts) have been encountered on large North-Sea semi-submersibles, including the Veslefrikk B platform in the Norwegian sector of the North Sea.

Air Gap Notation and Modeling Issues

Figure 1 shows a schematic view of a semi-submersible platform, both before and after waves are applied. In the absence of waves, the still-water airgap distance is denoted a_0. In the presence of waves, $\eta(t)$ denotes the wave surface elevation at a particular location along the structure, and $\delta(t)$ the corresponding vertical motion of the platform. If η=δ, the airgap would remain equal to its still-water value, a_0. More generally, the airgap response $a(t)$ will be reduced from a_0 by the difference, $\eta(t) - \delta(t)$:

$$\begin{aligned} a(t) &= a_0 - [\eta(t) - \delta(t)] \\ &= a_0 - r(t) \end{aligned} \tag{1}$$

in terms of the "relative wave" elevation

$$r(t) = \eta(t) - \delta(t) \tag{2}$$

While $\eta(t)$ records the wave with respect to a fixed observer, $r(t)$ may be viewed as the result that would be measured by a wave-staff attached to the moving structure at its still-water level. Deck impact occurs if the airgap $a(t) < 0$, or equivalently, if the relative wave $r(t)$ exceeds the still-water airgap a_0.

Among the various terms in Equation 1, the vertical offset $\delta(t)$ is perhaps the most simple to model. Linear diffraction results may often suffice to accurately model this offset. In contrast, the free surface elevation, $\eta(t)$, generally shows nonlinear behavior—and hence represents a non-Gaussian process. Much of our modeling attention is therefore focused here on $\eta(t)$.

Specifically, we assume $\eta(t)$ to be a sum of incident and diffracted waves, η_i and η_d, each of which is a sum of first- and second-order components:

$$\eta(t) = \eta_i(t) + \eta_d(t) \tag{3}$$

$$\eta_i(t) = \eta_{1,i}(t) + \eta_{2,i}(t) \tag{4}$$

$$\eta_d(t) = \eta_{1,d}(t) + \eta_{2,d}(t) \tag{5}$$

This is consistent with most state-of-the-art nonlinear hydrodynamic analyses, which employ second-order perturbation solutions.

Comparing the terms in Equations 3–5, note that $\eta_{1,d}$ requires only (relatively straightforward) linear diffraction analysis. It has been shown for this platform, however, that linear diffraction models underestimate extreme airgap response levels (Winterstein and Sweetman, 1999). In contrast, $\eta_{2,d}$ is far more difficult to compute. Second-order diffraction analyses are available (e.g., WAMIT, 1995), and have been found to notably increase predicted extremes of the near-structure wave surface (Manuel and Winterstein, 1999). As yet, however, these second-order results lack widespread use and verification in modeling the nonlinear diffracted wave surface.

As a result, the feasibility of a "hybrid" model is explored here. This model neglects the second-order diffraction term $\eta_{2,d}$, but retains the second-order incident wave term $\eta_{2,i}$. This term is available analytically from second-order Stokes theory. This is clearly a simplification which is likely to underestimate near-column diffraction effects; a goal here is to understand the numerical impact of this simplification. Two different stochastic models are then used: (1) a moment-based model which neglects the effect of $\eta_{2,d}$ on skewness and kurtosis; and (2) a narrow-band model which neglects the effect of $\eta_{2,d}$ only during the single largest wave cycle.

Description of Model Test Data

Test data considered here come from a 1:45 length-scale model of Veslefrikk, which was tested in the wave tank at Marintek using various types of irregular waves (Fokk, 1995). Figure 2 shows a plan view of the platform, together with the 9 locations

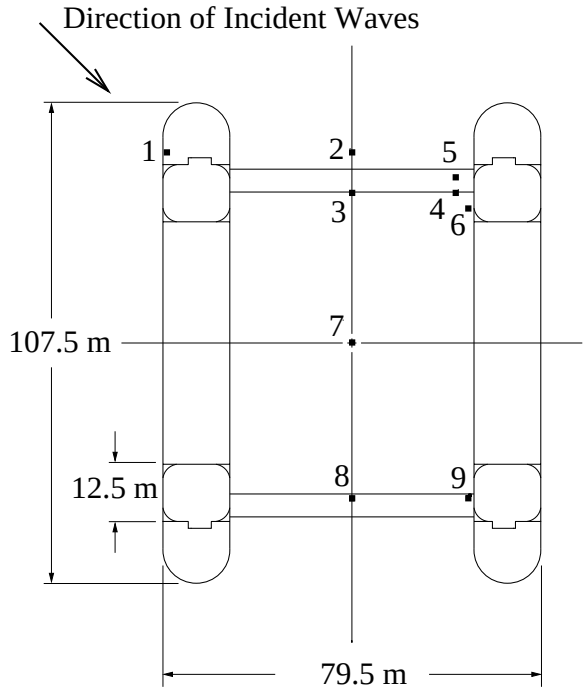

Figure 2. Plan view of Veslefrikk platform and location of air gap probes.

for which the air gap responses have been measured as a function of time. Note that airgap probes with lower numbers are generally further up-stream, i.e., closer to the wave generator. All tests studied here apply long-crested waves traveling along the diagonal of the structure.

The platform rigid-body motions in heave, roll, and pitch—denoted ξ_3, ξ_4, and ξ_5—have also been recorded. This permits estimation of the net vertical displacement $\delta(t)$ at any field-point location (x,y) of interest:

$$\delta(t) = \xi_3(t) + y \cdot \sin(\xi_4(t)) - x \cdot \sin(\xi_5(t)) \qquad (6)$$

Finally, from this estimate of $\delta(t)$ and the measured air gap history $a(t)$, Equations 1–2 can be used to infer $\eta(t)$ and $r(t)$, the absolute and relative wave elevation histories for the wave tank tests.

Table 1 summarizes the geometric properties of the platform. Tests have been run for two different draft levels: d=23m and d=26m. The cases with deeper draft reflect the original Veslefrikk operating conditions, during which wave impact with the underside of the deck was observed in the field (and reproduced in these model tests). Results for the survival draft, d=23m, are studied in detail here because the data has not been corrupted by impact with the deck at the airgap probe locations.

The waves are first generated in the model test basin before the model is placed in the basin. The incident wave, $\eta_i(t)$, is measured at location 7 (Figure 2), where the platform is to be centered. Following common practice, wave histories have been generated from a stationary random process model, applied over a fixed "seastate" duration of T_{ss}=3 hours. Its spectral density function, $S_\eta(f)$, is described by the significant wave height H_S=4σ_η, the peak spectral period, T_P, and the spectral peakedness factor γ. Three different test conditions were performed for the d=23m draft; Table 2 describes the H_S, T_P, and γ values for each of the three test conditions.

Platform Particulars	
Length Over All (LOA):	107.50 m
Longitudinal Column Spacing:	68.00 m
Transverse Column Spacing:	67.00 m
Column Length w/o Sponson:	12.50 m
Column Breadth:	12.50 m
Pontoon Breadth:	14.25 m
Pontoon Height:	9.50 m
Survival Conditions	
Draft, D:	23.00 m
Displacement:	40,692 tonnes
Airgap to Still Water Level:	17.50 m
Center of Gravity (from keel):	24.13 m
Pitch Radius of Gyration:	33.76 m
Roll Radius of Gyration:	34.26 m
Transverse Metacentric Height:	2.36 m
Water Depth:	175.00 m

Table 1. Characteristics of Veslefrikk platform.

H_S [m]	T_P [s]	γ	Number of 3-hour tests	Spectral Type
12.0	11.5	4.0	5	Bimodal
14.0	13.5	3.0	6	JONSWAP
15.5	16.5	2.0	2	JONSWAP

Table 2. Seastate parameters for which model tests were conducted.

Water Surface Elevation Relative to Earth (Vessel Motions Excluded)						Water Surface Elevation Relative to Moving Vessel				
	Standard Deviation (σ)	Skewness	Kurtosis	Cycle Rate (Hertz)	Peak Factor (Peak/σ)	Standard Deviation	Skewness	Kurtosis	Cycle Rate (Hertz)	Peak Factor (Peak/σ)
Airgap 1	3.98	0.385	3.510	0.0972	4.99	3.60	-0.08	3.47	0.0955	4.48
Airgap 2	3.09	0.242	3.164	0.0934	4.48	2.28	0.15	3.18	0.1013	4.67
Airgap 3	3.04	0.268	3.091	0.0934	4.43	2.22	0.18	3.19	0.1038	4.84
Airgap 4	3.43	0.424	3.296	0.1001	4.70	2.73	0.33	3.21	0.1086	4.77
Airgap 5	3.28	0.721	3.638	0.1014	5.41	2.56	0.76	3.53	0.1112	5.72
Airgap 6	3.27	0.430	3.452	0.1018	5.00	2.56	0.35	3.45	0.1128	5.12
Airgap 7	3.02	0.302	3.200	0.0941	4.55	2.23	0.25	3.27	0.1066	4.92
Airgap 8	3.35	0.343	3.180	0.0920	4.62	2.55	0.40	3.38	0.1011	4.98
Airgap 9	3.65	0.033	3.321	0.0989	4.29	2.89	0.35	3.73	0.1084	4.72
Measured Incident Wave	2.99	0.21	3.26	0.0882	4.77	2.99	0.21	3.26	0.0882	4.77
Calculated from 5 separate 3-hour seastate realizations H_s: 12.0 T_p: 11.5 Draft: 23 m										

Table 3. Absolute and Relative Wave Statistics

Statistical Description of Model Test Results

Table 3 shows statistics calculated from the model basin test data. Some of these statistics are repeated in Figures 3 – 6, which are discussed later. The first four statistical moments: mean, m_x (not shown in tables), standard deviation, σ_x, skewness, α_{3x}, and kurtosis, α_{4x} , are calculated from the data set as:

$$m_x = \mathrm{E}[x(t)] \tag{7}$$

$$\sigma_x^2 = \mathrm{E}[(x(t) - m_x)^2] \tag{8}$$

$$\alpha_{3x} = \frac{1}{\sigma_x^3}\mathrm{E}[(x(t) - m_x)^3] \tag{9}$$

$$\alpha_{4x} = \frac{1}{\sigma_x^4}\mathrm{E}[(x(t) - m_x)^4] \tag{10}$$

Here the "E" notation signifies the expectation (or averaging) operation. For a Gaussian process, the skewness is 0 and kurtosis is 3. The cycle rate is calculated as the number of times the water surface elevation up-crosses the mean elevation divided by the elapsed time.

The standard deviation, skewness and kurtosis shown in the table are calculated for one concatenated history, which is made up of all five 3-hour realizations of the target seastate. The standard deviation indicates the gross amplitude of the process. Comparing results in Table 3, the effect of the motions is to lessen the standard deviations of the airgap response at all wave-probe locations. This reduction indicates the correlation between the wave and the resulting vessel motions.

The skewness coefficient is a measure of the asymmetry of the response; a Gaussian process has zero skewness, reflecting peak-trough symmetry on average. Non-zero skewness is indicative of a non-Gaussian process, with positive skewness indicating that peaks are larger on average than troughs. Again in view of Table 3, the effect of the motions is to lessen the skewness of the airgap response at most locations. Thus, motions reduce not only the gross amplitude of the responses, but also the degree of response asymmetry.

Airgap measurements taken farther up-stream on the moving vessel are found to show a reduction in skewness due to vessel motion while downstream locations show an increase in skewness. Probe number 7 is at the center of the vessel. Apparently the roll-pitch motion (pitch across the diagonal), which is phase-linked to the heave, strongly influences the skewness of the airgap response.

The kurtosis coefficient is a measure of how both tails of a symmetric process vary from those of a Gaussian process. Kurtosis values above the Gaussian value of 3 indicate both higher peaks and lower troughs. Trends in this non-Gaussian effect vary with wave-probe location: generally the largest kurtosis values are found immediately up-stream of columns, e.g. at locations 1, 5, and 9.

Average extremes of the process are calculated by averaging the (zero-mean) maximum wave elevation over each 3-hour history. The peak factor is then introduced as a dimensionless indicator of the extremes of the process. The peak factor is calculated as the average extreme, as defined above, divided by the standard

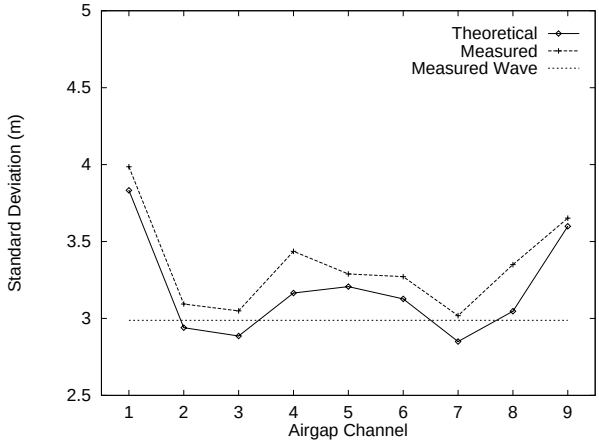

Figure 3. Standard Deviation

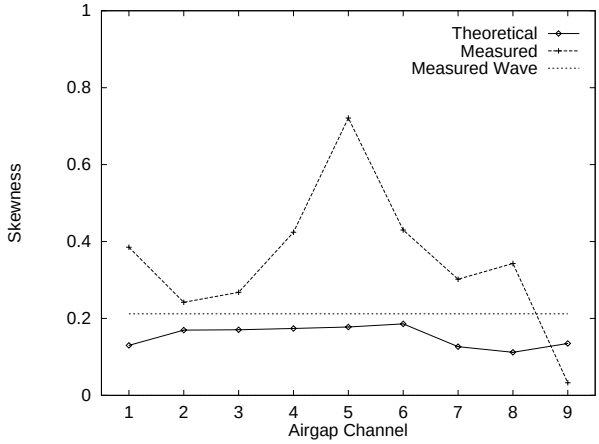

Figure 4. Skewness

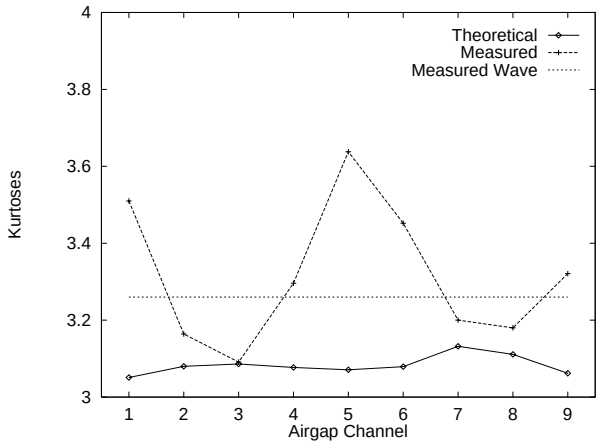

Figure 5. Kurtosis

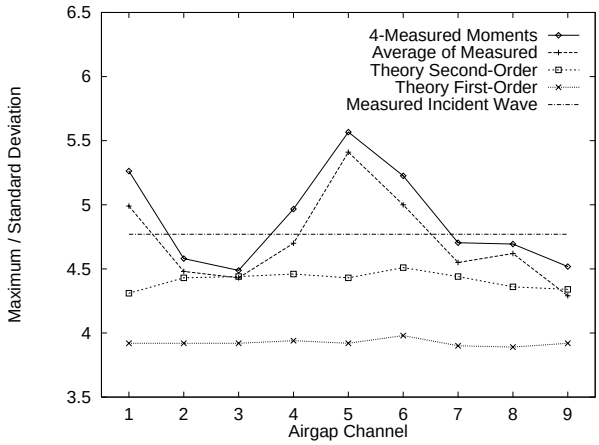

Figure 6. Peak Factor

Statistics of Wave and Airgap Response Processes

H_s=12 meters, T_p=11.5 seconds

deviation of the process. A Gaussian process has a peak factor of roughly $\sqrt{2\ln N)} + .577/\sqrt{2\ln N}$, in which N is the number of response cycles (Equation 15). Using a typical number of cycles in a 3-hour seastate, $N \approx 1000$, results in the peak factor ≈ 3.9. The larger peak factors in Table 3 reflect non-Gaussian behavior. A major goal here is to formulate and test peak factor estimates based on response moments—specifically skewness and kurtosis—or on a narrow-band model applied during the single most extreme wave cycle in the seastate.

Considering all the data presented in Table 3, the compensating effect of the vessel's floating atop the waves tends to lessen the extreme responses. More importantly the third and fourth statistical moments (skewness and kurtosis) become strong functions of location on the vessel relative to the direction of wave propagation, and which may be highly vessel-specific. Separation of the effects of vessel motion from those of hydrodynamic wave amplification enables a more pure analysis of those hydrodynamic effects. The remainder of this paper will focus exclusively on airgap response *calculated in absence of vessel motions*.

Theoretical Moment-Based Models and Results

Figures 3 – 6 compare the statistical moments and peak factors observed for $\eta(t)$ with those predicted from theory. In general, whether second-order diffraction effects are included or neglected, the first- and second-order processes $\eta_1(t)$ and $\eta_2(t)$ can

be rewritten in terms of standard Gaussian processes, $u_j(t)$:

$$\eta_1(t) = \sum_{j=1}^{2n} c_j u_j(t); \quad \eta_2(t) = \sum_{j=1}^{2n} \lambda_j u_j^2(t) \tag{11}$$

in which n is the number of frequency components of $\eta_1(t)$. The coefficients c_j and λ_j can be obtained by solving an eigenvalue problem of size n for problems involving difference or sum frequencies only (Næss, 1986, Næss, 1992), or of size $2n$ for problems—such as these airgap responses—which involve both (e.g., Winterstein et al, 1994). The resulting moments of η can be found directly from the coefficients c_j and λ_j:

$$\sigma_\eta^2 = \sum_{j=1}^{2n} (c_j^2 + \lambda_j^2) \tag{12}$$

$$\alpha_{3,\eta} = \frac{1}{\sigma_x^3} \sum_{j=1}^{2n} (6c_j^2\lambda_j + 8\lambda_j^3) \tag{13}$$

$$\alpha_{4,\eta} = 3 + \frac{1}{\sigma_x^4} \sum_{j=1}^{2n} (48c_j^2\lambda_j^2 + 48\lambda_j^4) \tag{14}$$

Equations 12–14 are used for the "theoretical" moment results shown in Figures 3–5.

Comparing first the standard deviation values from theory and measurement (Figure 3), good agreement is found in both magnitude and in behavior across the 9 field-points. Recalling that the theoretical results neglect second-order diffraction effects, it appears that linear diffraction may be sufficient to accurately predict the rms level of the wave elevation, and hence that of the air gap response.

Figures 4 and 5 show similar comparisons for the third and fourth statistical moments, respectively. Recalling that the *only* source of non-Gaussian behavior in the theoretical model is the incident wave, it is not surprising that these theoretical moments are relatively constant across field points. The best result that could be reasonably expected is that the theoretical higher moments roughly equal those of the incident wave. In fact, the second-order theory appears to accurately predict the wave skewness, but under-estimates its kurtosis (roughly 3.1 vs 3.3). This finding is consistent with a detailed Ph.D. study of second-order random waves (Jha, 1997; Jha and Winterstein, 2000). Beyond the theoretical underestimation of the "background" kurtosis level of the incident wave, the most striking feature of these figures is the strongly enhanced nonlinear behavior (increased skewness and kurtosis) observed at near-column locations (e.g., locations 1 and 5). It is clear that this nonlinear location-specific behavior cannot be modeled through linear diffraction alone.

Figure 6 shows the resulting moment-based predictions of the peak factor (average 3-hour extreme normalized by the response standard deviation). The "Theory First-Order" result uses a Gaussian random process model, for which the expected maximum of a standard Gaussian process, $U(t)$=$\eta(t)/\sigma_\eta$, in N cycles is estimated as

$$E[U_{max}] = \frac{E[\eta_{max}]}{\sigma_\eta} = \sqrt{2\ln N} + \frac{0.577}{\sqrt{2\ln N}} \tag{15}$$

The resulting peak factor, $E[\eta_{max}]/\sigma_\eta$, is consistently underestimated by Gaussian theory: predictions less than 4.0 compared with measurements of 4.5 to 5.5.

The "Theory Second-Order" results estimate extremes from a non-Gaussian (Hermite) model, using the theoretical skewness and kurtosis estimates from the preceding figures. Specifically, this model assumes the non-Gaussian process $\eta(t)$ to be a cubic transformation of a standard Gaussian process $u(t)$, conveniently rewritten as a sum of Hermite polynomials:

$$\eta = g(u) = \kappa\sigma_x[u + c_3(u^2 - 1) + c_4(u^3 - 3u)] \tag{16}$$

The variance of η is preserved by setting κ=$[1 + 2c_3^2 + 6c_4^2]^{-1/2}$. The coefficients c_3 and c_4 are determined to preserve the desired skewness and kurtosis. (Results presented in this paper are calculated using a numerical routine to "optimize" c_3 and c_4, to minimize error in matching skewness and kurtosis values; e.g., Winterstein et al, 1994). Assuming the same transformation g in Equation 16 applies at all points in time, the same transformation is applied to relate $E[\eta_{max}]$ to $E[U_{max}]$:

$$E[\eta_{max}] \approx g(E[U_{max}]) \tag{17}$$

Equations 15–17 serve as the basis of the "Theory Second-Order" results in Figure 6.

As might be expected, the peak factor estimates from second-order theory are always superior to the Gaussian results in Figure 6. Nonetheless, these second-order predictions fail to adequately follow the trend in observed extremes at near-column locations. This pattern of deviation, between measured peak factors and second-order predictions, closely follows the pattern of deviation in skewness and kurtosis from the preceding figures. Finally, Figure 6 also shows peak factor predictions using the actual four moments of the measured history. The relatively good agreement suggests that accurate moment estimates can lead to improved estimates of extremes. It may be valuable to use empirical models, such as the Hermite model, and then fitting statistical moments to observed data as functions of seastate parameters H_s and T_p.

Narrow-Band Model

To summarize, Figures 4–5 show that if second-order diffraction effects are not available, the resulting skewness α_3

and kurtosis α_4 of the wave surface will be underestimated. The model cannot predict the enhanced nonlinear effects (larger α_3, α_4) at near-column locations. As a result, using these moment estimates leads to a similar underestimation of extreme wave levels (Figure 6).

In contrast, Figure 3 shows that the standard deviation of the wave surface is accurately predicted with only first-order diffraction effects. Since $\eta_1(t)$ is a Gaussian process, knowledge of its standard deviation generally suffices to estimate its mean extreme (as in Equation 15):

$$E[\eta_{1,max}] = \sigma_{\eta_1}[\sqrt{2\ln N} + \frac{0.577}{\sqrt{2\ln N}}] \tag{18}$$

If the extreme of the total wave process, $\eta(t)$, is assumed to coincide in time with that of $\eta_1(t)$, it is only necessary to model second-order effects during that single, largest wave cycle. This is done below using a narrow-band random process model. The result thus neglects second-order diffraction effects only during the largest wave cycle, rather than during the entire seastate (as in the preceding moment-based model).

Applying a standard narrow-band model to the Gaussian process $\eta_1(t)$,

$$\eta_1(t) = a(t)\cos[\omega t + \theta(t)] \tag{19}$$

in terms of the slowly varying amplitude $a(t)$ and phase $\theta(t)$. (The instantaneous frequency ω may also be considered to be slowly varying.) The resulting second-order correction is then

$$\eta_2(t) = a^2(t)H_2^+(\omega,\omega)\cos 2[\omega t + \theta(t)] \tag{20}$$

in which H_2^+ is the second-order sum frequency transfer function. (The difference frequency transfer function, H_2^-, for a sinusoidal input gives only a constant offset, which does not contribute to oscillations about the mean wave surface.)

A key feature of Equations 19–20 is that they are assumed phase-locked; that is, in the largest wave cycle both processes are assumed to attain peak values at the same time (when both cosine terms are unity). At this time $a(t)$=$\eta_{1,max}$, so that the mean extreme of the total wave η=$\eta_1+\eta_2$ is estimated as

$$\begin{aligned} E[\eta_{max}] &= E[\eta_{1,max}] + E[\eta_{1,max}^2]H_2^+(\omega,\omega) \\ &\approx E[\eta_{1,max}] + E[\eta_{1,max}^2]\frac{k}{2} \end{aligned} \tag{21}$$

The latter approximation, $H_2^+ \approx k/2$ in terms of the wave number k, follows from the second-order Stokes model (again, second-order diffraction effects are neglected). This wave number k=ω^2/g should be based on a wave frequency "characteristic" of extreme waves. We choose here ω_c=$2\pi/(.92T_P)$, although results are expected to be relatively insensitive to this precise definition. Finally, Equation 18 is used to evaluate $E[\eta_{1,max}]$, while $E[\eta_{1,max}^2]$ is estimated as

$$E[\eta_{1,max}^2] = E[\eta_{1,max}]^2 + \frac{\pi^2}{6}\frac{\sigma_{\eta_1}^2}{2\ln N} \tag{22}$$

The last term in this result estimates the variance of $\eta_{1,max}$ (e.g., Madsen et al, 1986).

Comparison of All Models and Data

Figures 7 and 8 compare the observed mean extreme wave elevation with the predictions from all three preceding models. These predictions come from the conventional linear, moment-based nonlinear, and the narrow-band models (given respectively by Equation 15, Equations 15–17, and Equation 21). Results for the first two models have already been given, in terms of peak factors, for the H_S=12m seastate in Figure 6. Figures 7 and 8 show all results in terms of the mean extreme level, and for both H_S=12m and H_S=14m seastates. Recall that all three methods rely on the same first-order hydrodynamic analysis results.

As noted earlier, the standard linear model is generally non-conservative, underpredicting the airgap demand for all wave probe locations and for both seastates. The air gap demand extremes are typically underpredicted (compared with "Observed") by at least 20%, and sometimes substantially more, particularly at the near-column locations. Recall from Figure 3 that the RMS response of the process is typically underpredicted by 10% or less.

Both the moment-based and narrow-band models are substantially more accurate than the standard linear model. With respect to the moment-based model, the underprediction of α_3 and α_4 (Figures 4 and 5) propagate through the analysis, so that the extremes of the process are also somewhat underpredicted. Extreme estimates from the narrow-band model are generally found to be somewhat more accurate, better following the observed spatial variability (e.g., at the near-column locations 1 and 9). The air gap demand at location 5 is still underpredicted, and behavior at this location has proven very hard to predict; wave impact at this location was found in the field and repeated in this set of model tests. At all locations and for both seastates, the narrow-band model performs better than either of the other methods.

Conclusions

Detailed model tests for the Veslefrikk semi-submersible platform have been studied. Motion and air gap time histories

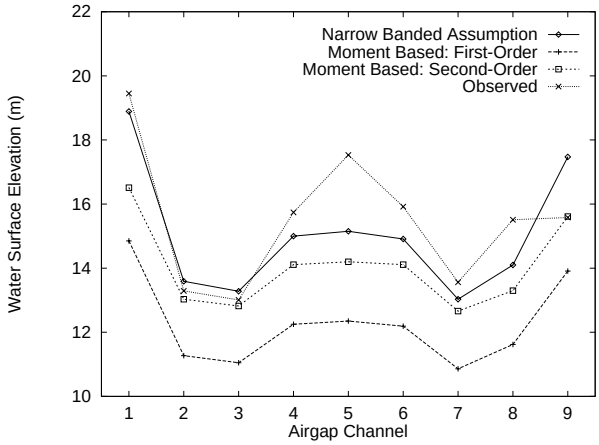

Figure 7. H_s = 12 meters, T_p = 11.5 seconds

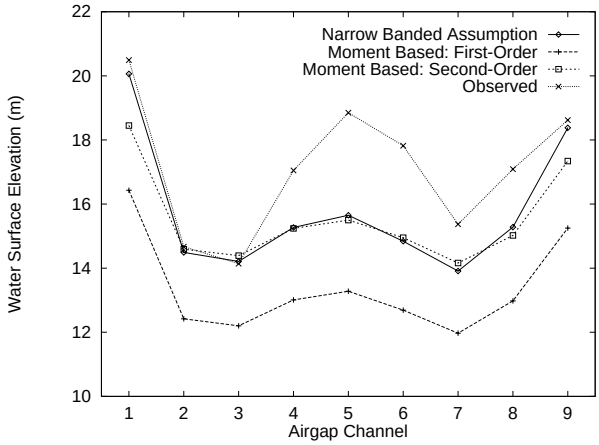

Figure 8. H_s = 14 meters, T_p = 13.5 seconds

η_{max} as Observed and Predicted by Various Methods

have been used to perform statistical analyses both for the absolute near-structure wave elevation (with respect to a fixed observer), and the relative wave elevation (with respect to the moving structure), with the theoretical focus on the latter.

A standard linear diffraction model typical of common practice has been shown to underpredict the airgap demand for all wave probe locations. Air gap demand extremes are typically underpredicted by 20% or more, while the airgap demand standard deviation is typically underpredicted by 10% or less.

Two new models are proposed that include second-order effects in the incident waves, but that do not require the relatively difficult second-order diffraction calculations. The first model is moment-based and the second relies on narrow-band random process theory. Either model can be implemented in place of the more standard linear-only model with little additional computational effort because only linear diffraction analysis is required. Either model better predicts the airgap demand than standard linear diffraction analysis.

The moment-based model requires an eigenvalue analysis to determine the statistical moments of the resulting non-Gaussian process. The skewness and kurtosis, α_3 and α_4, are underpredicted in absence of second-order diffraction effects. The extremes of the process are conveniently predicted from these moments using Hermite models. Despite the under prediction and insufficient spatial variability of the extremes associated with underestimation of α_3 and α_4 (Figures 3–6), this model better predicts the air gap demand than standard linear theory.

The narrow-band model is derived by neglecting second-order diffraction effects during only the largest wave cycle and by assuming the first and second-order parts of the wave cycle are phase locked. A relatively simple closed-form expression is found for direct estimation of extremes (Equation 22). Resulting extreme estimates are found to be more accurate and to better predict spatial variability than those resulting from either standard linear theory or the moment-based model (Figures 7 and 8).

Acknowledgements

This study is part of the doctoral work of the first author, within the Reliability of Marine Structures (RMS) program at Stanford University. The authors wish to thank all the project sponsors and especially Sverre Haver at Statoil, for making available the wave tank data, and Knut Engebretsen at Aker Engineering A.S., for making available the WAMIT hydrodynamic analysis of the Veslefrikk platform.

References

Fokk, T. (1995). Veslefrikk B air gap model tests. *Report 1383,* Marintek, Norwegian Marine Technology Research Institute.

Jha, A.K. (1997). *Nonlinear stochastic models for ocean wave loads and responses of offshore structures and vessels,* Ph.D. thesis, Civil Eng. Dept., Stanford University.

Jha, A.K. and S.R. Winterstein (2000). Nonlinear random ocean waves: prediction and comparison with data. *Proc., 19th Intl. Offshore Mech. Arctic Eng. Symp.,* ASME.

Madsen, H.O., S. Krenk, and N.C. Lind (1986). *Methods of structural safety,* Prentice-Hall, Inc., New Jersey.

Manuel, L. and S.R. Winterstein (1999). Air gap response of floating structures: statistical analyses from linear and nonlinear diffraction. *J. Offshore Mech. Arctic Eng.,* ASME, under review.

Næss, A. (1986). The statistical distribution of second-order slowly-varying forces and motions. *Appl. Ocean Res.,* **8**(2),

110–118.

Næss, A. (1992). Prediction of extremes related to the second-order, sum-frequency response of a TLP. *Proc., 2nd Intl. Offshore Polar Eng. Conf.*, ISOPE, 436–443.

WAMIT, 4.0 (1995). *WAMIT: a radiation-diffraction panel program for wave-body interactions–user's manual*, Dept. of Ocean Eng., M.I.T.

Winterstein, S.R. and B. Sweetman (1999). Air gap response of floating structures: statistical predictions vs observed behavior. *Proc., 18th Intl. Offshore Mech. Arctic Eng. Symp.*, ASME.

Winterstein, S.R., T.C. Ude and G. Kleiven (1994). Springing and slow-drift responses: predicted extremes and fatigue vs. simulation. *Proc., BOSS-94*, **3**, Massachusetts Institute of Technology, 1–15.

Winterstein, S.R., T.C. Ude and T. Marthinsen (1994). Volterra models of ocean structures: extreme and fatigue reliability. *J. Engrg. Mech.*, ASCE, **120**(6), 1369–1385.